GNR Based Reconfigurable Tapered Vivaldi Antenna for THz band Applications

Ritesh Kumar Kushwaha[1,1*]

[1*]ECE, Chandigarh University, Gharuan, Mohali, 140413, Punjab, India.

Corresponding author(s). E-mail(s): riteshkushwaha04@gmail.com;

Abstract

This article presents a novel high gain Tapered Vivaldi antenna (TVA) utilizing Graphene Nano Ribbon (GNR) for the Terahertz band applications. The proposed design based on substrate extension technique and graphene hybrid metal structure to improve the radiation characteristics. It also derives the Electric and Magnetic field of graphene is systematically using FDTD numerical modeling. The reconfigurability properties of antenna can be achieved by changing the chemical potential. The result offers a minimum return loss of -58.68 dB, an impedance bandwidth of 298.84 GHz, a peak gain of 12.31 dBi, peak directivity of 13.1 dBi, and radiation efficiency of 83.63 %. The investigated results reveals the better results within the preferred frequency band. Therefore, the designed antenna can be useful for various THz applications.

Keywords: TSA,GNR, frequency reconfiguration, FDTD, THz band

1 Introduction

With the advancement of sub-millimeter wave technology, it has been seamless attention in this frequency regime from 0.3 THz to 3 THz, which lies in the spectrum between microwave wave and visible light. The millimeter-wave technology has been significantly suitable for science, medical imaging, high data rate wire- less communications, security, etc. [1]. An antenna is a key component in the millimeter-wave technology that fascinated lots to the research community. It has projected various types of antennas to blow 60-GHz [2]. Nevertheless, horn-antennas were the finest option to attain maximum gain due to restricted fabrication and measurement facilities in the mm-wave frequency range up to 60 GHz [3]. Conversely, several fabrication technologies including SIW, MEMs and LTCC reduce the volume of the conventional horn antennas [4-5]. Remarkably, ultra-wideband (UWB) antennas significantly reduce the imprint of a system by substituting multiple and multi-band antennas conventionally required to include various bands [6]. In this view, Vivaldi antennas have been extensively used to obtain a wide band frequency range as an end-fire antenna. Initially Gibson [7] projected the Vivaldi in the year 1979 and then extensive research were reported utilizing numerous design methods in the GHz to millimeter frequency range [8-11].

However, some Tapered Vivaldi antennas (TSA) have been presented in the THz band. In recent years, photoconductive Vivaldi antenna has been presented over the frequency band from 1-to-6 -THz frequency. However, wideband is achieved by utilizing a hemisphere lens, but it observed poor gain and radiation efficiency [12]. Rmili et al. [13], reported an ultra-wideband Vivaldi antenna with a gain of around -5 dBi and radiation efficiency of around 16

On the other hand, graphene material is observed as a very suitable candidate for achieving reconfigurability in the THz frequency band due to its high electron mobility and controlling mechanism. In [15], a Reconfigurable THz Vivaldi antenna was reported using a graphene-metal hybrid structure and observed the peak gain around 7-dBi. In a similar work, authors [16] had achieved a peak gain of around 13 dB, and the reconfigurable nature of Vivaldi antenna using hyperbolic metamaterial placed on the extended substrate over the frequency band from 0.5-to-2-THz. However, designing constraints of hyperbolic structure exist.

Unlike the above technique, reconfigurable Vivaldi antenna and improved gain are still needed in the THz frequency band. This paper proposes a simple Tapered Vivaldi antenna with extended substrate and reconfigurable characteristics for 0.5 to 0.9 THz applications. The rest of the article is arranged as follows: Section II, covers the conventional TS antenna designing techniques and Parametric study. Section III describes the graphene's surface conductivity, Modelling, and reconfigurable properties in the THz band. The simulation results of the projected design are in Section IV. Finally, the summary and conclusion of the work are presented in Section V.

2 Antenna Geometries and Analysis

Fig.1 shows the design of a Tapered antenna (Ant-1) employed on a 10 μm Quartz substrate with a dielectric constant of 3.78. In the initial design two flared linear arms are realized from the Tapered slot named as Step-constant Tapered antenna. With the reference of starting point (P1) and end point (P2) the profile is described by:

$$y = c_1 k_t x \tag{1}$$

From the Linear tapered line in the point P_1 and the point P_2, we obtain the constant c_1 and opening rate k_t:

$$c_1 = S/2 \tag{2}$$

$$k_t = 1/L_t(W_t/S) \tag{3}$$

Where $'S' = slotlinewidth$, $W_t = Taperedwidth$, and L_t is the Tapered length. Further, the overall width (W_p) and length (L_p) of the Vivaldi antenna can be expressed by:

$$W_p = ((2M + 1)c)/(2f_m insqrt(\varepsilon_r)) \tag{4}$$

$$L_p = ((2N+1)\lambda_0)/(2\sqrt{(}\varepsilon_e ff\ ))+0.842\times h\ ((0.3+\varepsilon_e ff))/((0.258-\varepsilon_e ff))\ ((W_t+0.264\times h)) \tag{5}$$

Where M, N is the positive constant for this design, we consider M = 1 and N = 3. Also, c = speed of light, $f_m in$ = lowest operating frequency, λ_0 = resonance wavelength, ε_r = permittivity of a substrate, ε_{eff} = substrate effective permittivity.

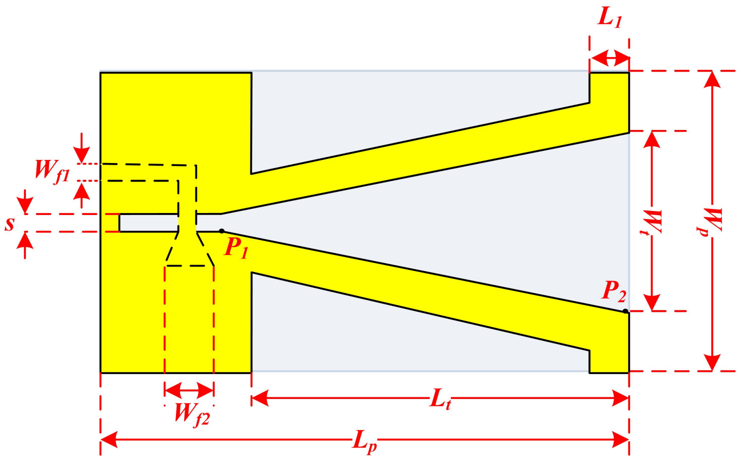

Fig. 1: Geometry of Tapered Vivaldi antenna (Ant-1)

Subsequently, the particle swarm optimization (PSO) technique is adopted to achieve the desired -10 dB impedance bandwidth over the operating frequency range.

Fig.2(a) illustrates the variation of a reflection coefficient by changing the slot's width, such as $10\mu m$,$12\mu m$,$14\mu m$,$16\mu m$,and $18\mu m$. One can see that optimum bandwidth and the reflection coefficient are achieved at the slot width of $10\mu m$. Fig.2 (b) illustrates the performance of a s-parameter by changing the tapered widths of 304.2μm, 324.2μm, 344.2μm, 364.2μm, and 384.2μm. It reveals that the optimum reflection coefficient is achieved with a tapered width of 384.2 μm. Moreover, to obtain the appropriate matching of impedance, the stub width of feed-line is investigated. The influence of changing the stub width is illustrated in Fig.2 (c). It should be notice that the optimum value of impedance bandwidth and reflection coefficient is obtained at 50.3 μm. Further, L1 is varied to analyze the effect of the targeted parameter, however it is no such significant changes has been seen in Fig.2(d). Finally, the optimum dimensions of a tapered antenna are illustrated in Table 1.

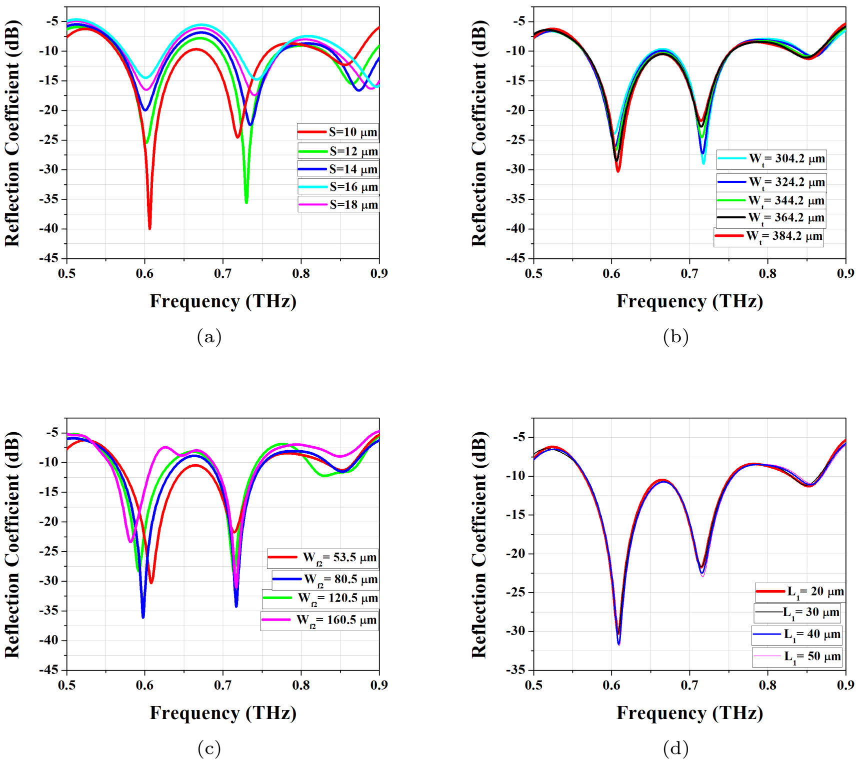

Fig. 2: Impact of S-parameter by varying (a) Slots width (b) Aperture Width (c) Feed Width and (d) length of L_1

The designed Tapered antenna (Ant-1) is further modified in the structure to investigate the radiation performance. The substrate structure is lengthening without changing the other parameter of Ant-1, as shown in Fig. 3(a). The

Table 1: Optimized dimension of Tapered antenna

Parameters	**Symbol**	**Dimension (um)**
Tapered Length	Lt	630
Tapered Width	Wt	380
Antenna Length	Lp	800
Antenna Width	Wp	590
slot width	s	10
Feed-line Width	Wf1	20.47
Stub width	Wf2	53.50
Flared arm end width	L1	20

impact of lengthening of substrate in reflection coefficient and gain is illustrated in Fig. 3(b). The operating frequency range observed a minimum return loss of -45 dB and peak gain of 11.71 dB at an extended substrate of 500 μm.

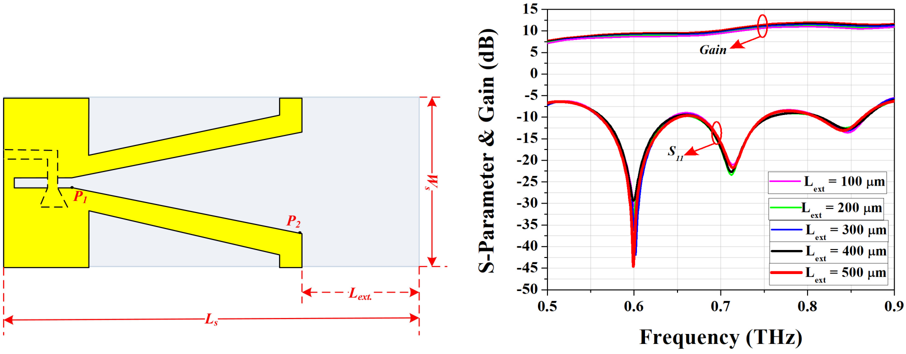

(a) (b)

Fig. 3: (a)Geometry of proposed Tapered antenna (ANT-2) with extended substrate (b) reflection coefficient and gain behavior with extended substrate

3 Surface conductivity and Graphene Modelling at THz Frequency

Graphene is a mono-layered carbon atom arranged in a honeycomb lattice structure. Its extraordinary feature like high electron mobility and supporting nature of surface plasmon polariton (SPP) wave make graphene an excellent candidate for the various THz applications [17]. The graphene's conductivity can be computed by Kubo's formulation [18] and considered the intra-band conductivity here due to operating frequency ranges below the 30-THz band [19]. The intra-band surface conductivity can be expressed as:

$$\sigma\left(\omega,\Gamma,\mu_c,\ T\right)_{intra,\ s} = \frac{jk_BTe^2}{\left(-\omega+j2\Gamma\right)\pi\hbar^2}\left[\frac{\mu_c}{k_BT}+2\ ln\left(e^{-\frac{\mu_c}{k_BT}+1}\right)\right] \tag{6}$$

Where, $\sigma\left(\omega\right)_{intra,\ s}$ is the surface intraband conductivity, ω = angular frequency, K_B = Boltzmann constant, e = charge of electron, T = temperature, $\hbar$ = reduced plank-constant, μ_c = chemical-potential, Γ = effective scattering-rate and relaxation time $(\tau) = 1/\Gamma$.

The impact of surface conductivity behavior with various chemical potential can be analyzed in Fig.4

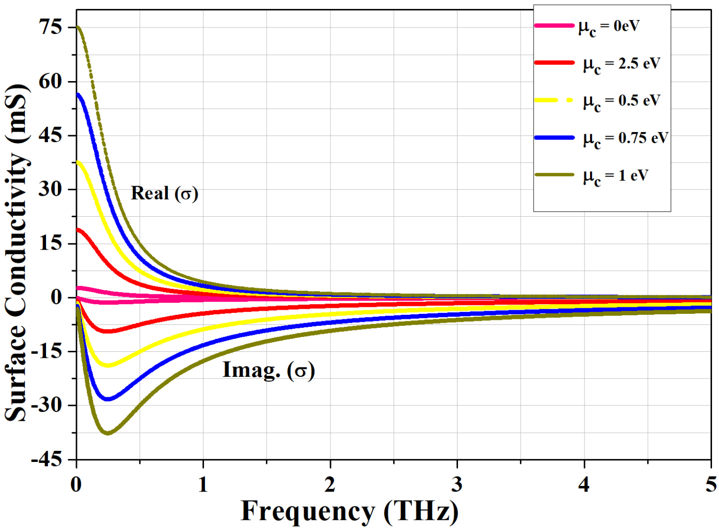

Fig. 4: Surface conductivity of graphene with various chemical potential.

After confirming the reconfigurable nature, graphene nano ribbon (GNR) can be used to achieve the frequency reconfiguration property and to improve the radiation characteristics of a proposed ANT-2. Fig. 5 shows the geometry of antenna design. As per the available literature, graphene can be grown on the copper metal called graphene-metal structures and on the quartz substrate by using the chemical vapour deposition (CVD) Method [21-22].

Here, GNR is designed on the top of the metallic Vivaldi and also placed parallel to the flared arm structure to improve the surface current. The width of GNR plated on the copper is 5 μm, the width of parallel GNR is 15 μm, and the periodicity of a parallel GNR structure is 25 μm.

In addition, to investigate the current density, electric field and magnetic field of graphene, the Finite Domain Time Difference (FDTD) is used [20]. This technique discretization Volume and then apply the Perfectly Matched

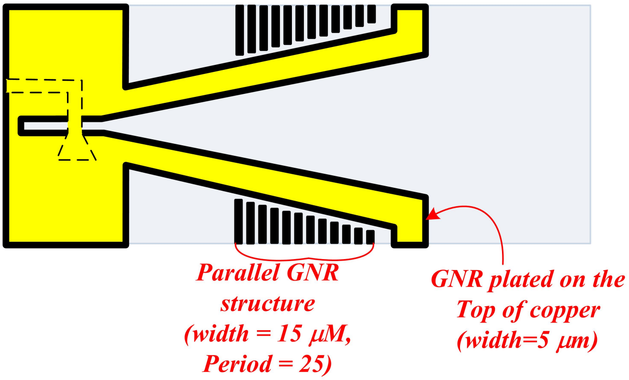

Fig. 5: Geometry of GNR based Tapered Vivaldi antenna structure

Layer (PML) method to compute the parameters described as follows: The volumetric conductivity of graphene is then expressed by:

$$\sigma_{intra,v} = \frac{\sigma_{intra,s}}{tg} = \frac{D}{2\Gamma + j\omega} \tag{7}$$

where, tg= thickness of graphene and
$D = \frac{e^2 K_B T}{\pi \hbar^2} \left(\frac{\mu_c}{K_B T} + 2ln(e^{-\frac{\mu_c}{K_B T}}) \right) / t_g$
The current density 'J' of graphene is expressed by:

$$\overline{J} = \sigma_{intra,v} \overline{E} = \frac{D}{2\Gamma + j\omega} \overline{E} \tag{8}$$

$$or, \frac{\partial}{\partial t} \overline{J} + 2\Gamma \overline{J} = D\overline{E} \tag{9}$$

Discretization of Current density, electric field, and partial derivative in integer time steps 'n' :

$$\frac{(\overline{J}^{n+1} - \overline{J}^{n})}{\Delta t} + 2\Gamma \frac{(\overline{J}^{n+1} + \overline{J}^{n})}{2} = D \frac{(\overline{E}^{n+1} + \overline{E}^{n})}{2} \tag{10}$$

$$or, \overline{J}^{n+1} = \left[\frac{1 - \Gamma \Delta t}{1 + \Gamma \Delta t} \right] \overline{J}^{n} + \frac{D \Delta t}{2(1 + \Gamma \Delta t)} (\overline{E}^{n+1} + \overline{E}^{n}) \tag{11}$$

$$\overline{E}^{n+1} = \overline{E}^{n} - \frac{\Delta t}{\epsilon} \Delta \times \overline{H}^{n+\frac{1}{2}} - \frac{\Delta t}{2\epsilon} \left(\overline{J}^{n+1} + \overline{J}^{n} \right) \tag{12}$$

$$\overline{E}^{n+1} = \frac{1}{M} \left[N \cdot \overline{E}^{n} - \frac{\overline{J}^{n+1}}{(1 + \Gamma \Delta t)} \right] - \Delta \times \overline{H}^{n+\frac{1}{2}} \tag{13}$$

Where M $= \frac{\varepsilon}{\Delta t} + \frac{D \Delta t}{4(1+\Gamma \Delta t)}$ and N $= \frac{\varepsilon}{\Delta t} - \frac{D \Delta t}{4(1+\Gamma \Delta t)}$

The Yee's cell [23] techniques has been used to a discretized spatial domain in $\Delta x \times \Delta y \times \Delta z$ dimension which considering a unit cell as depicted in Fig.6.

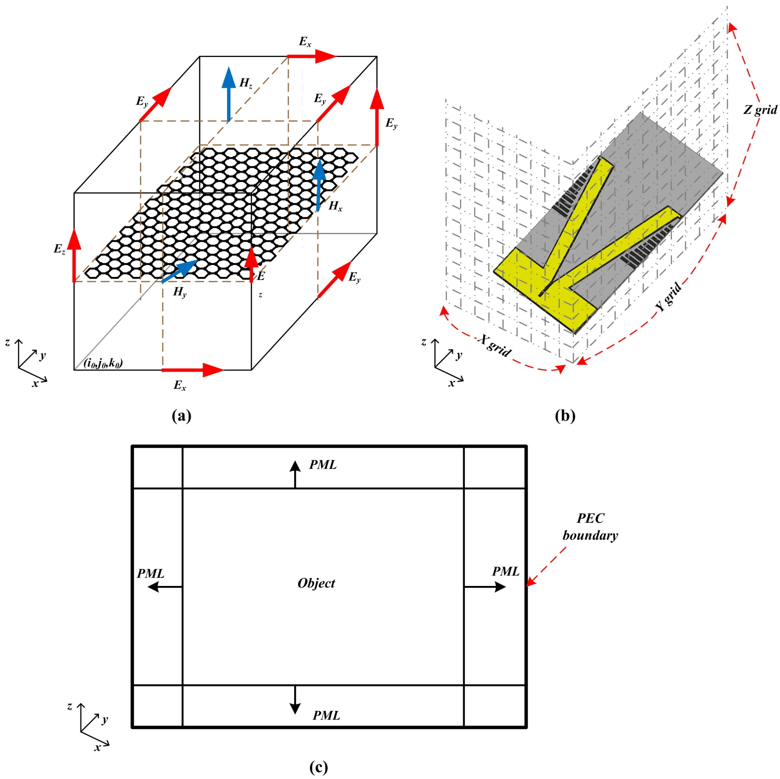

Fig. 6: (a) 3D Yee's-cell distribution of Graphene sheet (b) Proposed GNR based Vivaldi antenna (c) PML Boundary in xy plane.

All fields are primarily positioned to zero in the simulation domain. With a source excitation, all Magnetic fields (H) and Electric fields (E) are upgraded at the integer time step n+0.5, n respectively. Reiterating this process yields the simulation to stride in time. Similarly, the other E fields and H fields can be derived. Hence, the FDTD update equations are:

$$\begin{aligned}
&E^{n+1}_{x,[(\vec{i_0}+\frac{1}{2}),\vec{j_0},\vec{k_0}]} = \frac{1}{M}\Bigg[N \cdot E^{n}_{x,[(\vec{i_0}+\frac{1}{2}),\vec{j_0},\vec{k_0}]} \\
&- \frac{1}{(1+\Gamma\Delta t)} J^{n+1}_{y,[(\vec{i_0}+\frac{1}{2}),\vec{j_0},\vec{k_0}]} \\
&+ \left(\frac{H^{n+\frac{1}{2}}_{z,[(\vec{i_0}+\frac{1}{2}),(\vec{j_0}+\frac{1}{2}),\vec{k_0}]} - H^{n+\frac{1}{2}}_{z,[(\vec{i_0}+\frac{1}{2}),(\vec{j_0}-\frac{1}{2}),\vec{k_0}]}}{\Delta y}\right) \\
&- \left(\frac{\overline{H}^{n+\frac{1}{2}}_{y,[(\vec{i_0}+\frac{1}{2}),\vec{j_0},(\vec{k_0}+\frac{1}{2})]} - H^{n+\frac{1}{2}}_{y,[(\vec{i_0}+\frac{1}{2}),\vec{j_0},(\vec{k_0}-\frac{1}{2})]}}{\Delta z}\right)\Bigg]
\end{aligned} \tag{14}$$

$$\begin{aligned}
&E^{n+1}_{y,[\vec{i_0},(\vec{j_0}+\frac{1}{2}),\vec{k_0}]} = \frac{1}{M}\Bigg[N \cdot E^{n}_{y,[[\vec{i_0},(\vec{j_0}+\frac{1}{2}),\vec{k_0}]} \\
&- \frac{1}{(1+\Gamma\Delta t)} J^{n+1}_{y,[\vec{i_0},(\vec{j_0}+\frac{1}{2}),\vec{k_0}]} \\
&+ \left(\frac{H^{n+\frac{1}{2}}_{x,[\vec{i_0},(\vec{j_0}+\frac{1}{2}),(\vec{k_0}+\frac{1}{2})]} - H^{n+\frac{1}{2}}_{x,[\vec{i_0},(\vec{j_0}+\frac{1}{2}),(\vec{k_0}-\frac{1}{2})]}}{\Delta z}\right) \\
&- \left(\frac{\overline{H}^{n+\frac{1}{2}}_{z,[(\vec{i_0}+\frac{1}{2}),(\vec{j_0}+\frac{1}{2}),\vec{k_0}]} - H^{n+\frac{1}{2}}_{z,[(\vec{i_0}-\frac{1}{2}),(\vec{j_0}+\frac{1}{2}),\vec{k_0}]}}{\Delta x}\right)\Bigg]
\end{aligned} \tag{15}$$

$$\begin{aligned}
&E^{n+1}_{y,[\vec{i_0},(\vec{j_0}+\frac{1}{2}),\vec{k_0}]} = \frac{1}{M}\Bigg[N \cdot E^{n}_{y,[[\vec{i_0},(\vec{j_0}+\frac{1}{2}),\vec{k_0}]} \\
&- \frac{1}{(1+\Gamma\Delta t)} J^{n+1}_{y,[\vec{i_0},(\vec{j_0}+\frac{1}{2}),\vec{k_0}]} \\
&+ \left(\frac{H^{n+\frac{1}{2}}_{x,[\vec{i_0},(\vec{j_0}+\frac{1}{2}),(\vec{k_0}+\frac{1}{2})]} - H^{n+\frac{1}{2}}_{x,[\vec{i_0},(\vec{j_0}+\frac{1}{2}),(\vec{k_0}-\frac{1}{2})]}}{\Delta z}\right) \\
&- \left(\frac{\overline{H}^{n+\frac{1}{2}}_{z,[(\vec{i_0}+\frac{1}{2}),(\vec{j_0}+\frac{1}{2}),\vec{k_0}]} - H^{n+\frac{1}{2}}_{z,[(\vec{i_0}-\frac{1}{2}),(\vec{j_0}+\frac{1}{2}),\vec{k_0}]}}{\Delta x}\right)\Bigg]
\end{aligned} \tag{16}$$

The $\overline{H}$ fields can be updated as:

$$H^{n+\frac{1}{2}} = H^{n-\frac{1}{2}} - \frac{\Delta t}{\mu}\Delta \times E^{n+\frac{1}{2}} \tag{17}$$

The discretized 3-D update equations for graphene are listed below:

$$H^{n+\frac{1}{2}}_{x,[\vec{i_0},(\vec{j_0}+\frac{1}{2}),(\vec{k_0}+\frac{1}{2})]} = H^{n-\frac{1}{2}}_{x,[\vec{i_0},(\vec{j_0}+\frac{1}{2}),(\vec{k_0}+\frac{1}{2})]} - \frac{\Delta t}{\mu}\left(\frac{E^n_{z,[\vec{i_0},(\vec{j_0}+\frac{1}{2}),(\vec{k_0}+\frac{1}{2})]} - E^n_{z,[\vec{i_0},\vec{j_0},(\vec{k_0}+\frac{1}{2})]}}{\Delta y}\right) - \left(\frac{E^n_{y,[\vec{i_0},(\vec{j_0}+1/2),(\vec{k_0}+1)]} - E^n_{y,[\vec{i_0},(\vec{j_0}+\frac{1}{2}),\vec{k_0}]}}{\Delta x}\right) \tag{18}$$

$$H^{n+\frac{1}{2}}_{y,[(\vec{i_0}+\frac{1}{2}),\vec{j_0},(\vec{k_0}+\frac{1}{2})]} = H^{n-\frac{1}{2}}_{y,[(\vec{i_0}+\frac{1}{2}),\vec{j_0},(\vec{k_0}+\frac{1}{2})]} - \frac{\Delta t}{\mu}\left(\frac{\overline{E}^n_{x,[(\vec{i_0}+\frac{1}{2}),\vec{j_0},(\vec{k_0}+1)]} - E^n_{x,[(\vec{i_0}+\frac{1}{2}),\vec{j_0},\vec{k_0}]}}{\Delta z}\right) - \left(\frac{E^n_{z,[(\vec{i_0}+1),\vec{j_0},(\vec{k_0}+\frac{1}{2})]} - E^n_{z,[\vec{i_0},\vec{j_0},(\vec{k_0}+\frac{1}{2})]}}{\Delta x}\right) \tag{19}$$

$$H^{n+\frac{1}{2}}_{z,[(\vec{i_0}+1/2),(\vec{j_0}+\frac{1}{2}),\vec{k_0}]} = H^{n-\frac{1}{2}}_{z,[(\vec{i_0}+\frac{1}{2}),(\vec{j_0}+\frac{1}{2}),\vec{k_0}]} - \frac{\Delta t}{\mu}\left(\frac{E^n_{y,[(\vec{i_0}+1),(\vec{j_0}+\frac{1}{2}),\vec{k_0}]} - E^n_{y,[\vec{i_0},(\vec{j_0}+\frac{1}{2}),\vec{k_0}]}}{\Delta x}\right) - \left(\frac{E^n_{x,[(\vec{i_0}+\frac{1}{2}),(\vec{j_0}+1),\vec{k_0}]} - E^n_{x,[(\vec{i_0}+\frac{1}{2}),\vec{j_0},\vec{k_0}]}}{\Delta y}\right) \tag{20}$$

Thus, the propagation equations of E-field and H-field can be further upgraded by updated in y, z, and x grid. Moreover, the rest of the analytical domain without graphene is evaluated by utilizing the standard FDTD method. Here, the Perfectly Matched Layer (PML) scheme is utilized to simulate the design in free-space [24].

4 Result and Discussion

In this section reconfigurable nature of ANT-3 and compared results of all design will be discussed briefly.

4.1 Reconfigurable nature of proposed antenna

Fig.7 shows the reconfigurable characteristics of proposed Ant-3 by changing the different chemical potential. Fig. 7(a) illustrates the reconfigurable nature of reflection coefficient behavior over the frequency band from 0.5-to-0.9-THz band. Also, the optimum value can be seen at 0.75 eV. Fig. 7 (b) demonstrates the improving nature of gain with higher chemical potential values. However, the behavior of radiation efficiency varies indifferent and observed the values between 82-to-90 %, as seen in Fig. 7 (c). More specifically, the Real and Imaginary value of input Impedance behavior is presented in Fig. 7 (d) at 0.75 eV of chemical potential.

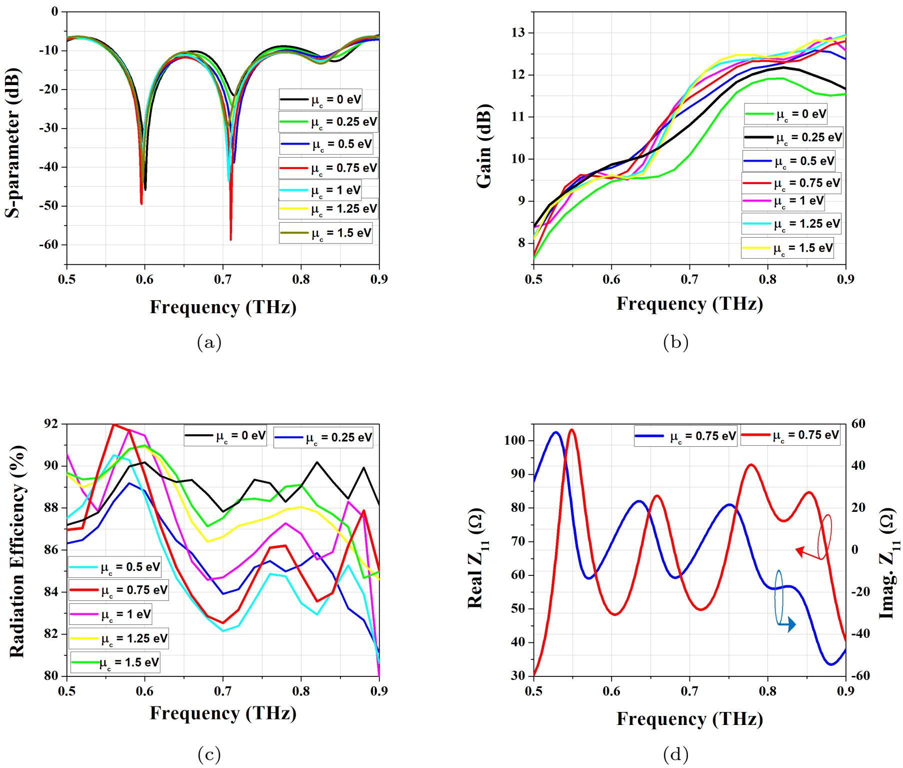

Fig. 7: Reconfiguration behavior of ANT-3 with different chemical potential (a) Reflection coefficient (b) Gain (c) Radiation efficiency (d) Real and Imaginary Input Impedance at 0.75 eV.

4.2 Comparison of the radiation characteristics of proposed design

After studying and ensuring the performance of planned antennas i.e., ANT-1, ANT-2, and ANT-3, the comparison of s-parameter behavior is exhibited in Fig.8. Fig.8 (a) reveals a minimum reflection coefficient of -58.68 dB at the 0.71-THz frequency with a maximum impedance bandwidth of 298.84 GHz for ANT-3. Also, ANT-1 and ANT-2 show impedance bandwidth of 187.73 GHz and 89.86 GHz, respectively. Moreover, ANT-2 illustrates the dual-band characteristics over the operating frequency range. Fig.8 (b) displays the comparative performance of proposed designs in which maximum gain is observed in the case of ANT-3. Further, Fig.8 (c) and Fig.8 (d) show the radiation efficiency and peak directivity comparison plot. The achieved Peak directivity of ANT-1, ANT-2, and ANT-3 are 10-dBi, 12.2-dBi, and 13.1 dBi. However, one can notice the less radiation efficiency for ANT-3 compared with ANT-1 and ANT-2, but the overall performance is significantly better.

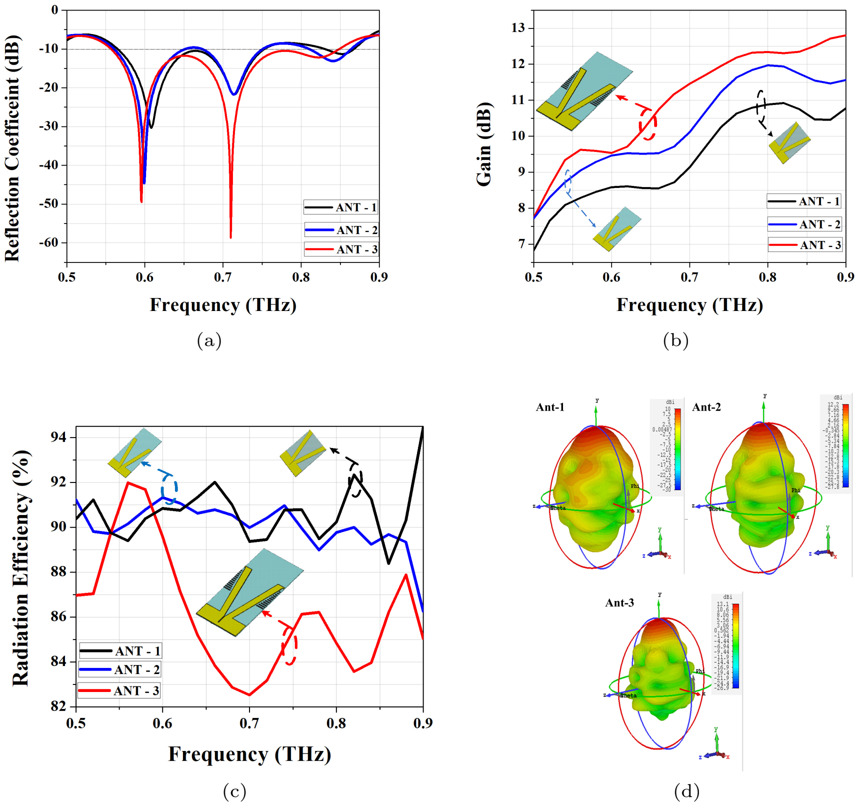

Fig. 8: Performance comparison of proposed designs (a) Reflection coefficient (b) Gain (c) Radiation efficiency (d) Peak directivity at resonance frequency of 0.71-THz (left-most) , 0.84-THz (middle) and 0.85-THz (right-most)

In order to further realize the performance of the proposed design, particularly at the resonance frequencies, the current distribution of the ANT-1, ANT-2, and ANT-3 is shown in Fig.9. As indicated in ANT-1(at 0.608

THz) and ANT-2 (at 0.71 THz) nearly have the similar current distribution. However, in case of ANT-3, more current is interlinked with GNR at 0.71-THz.

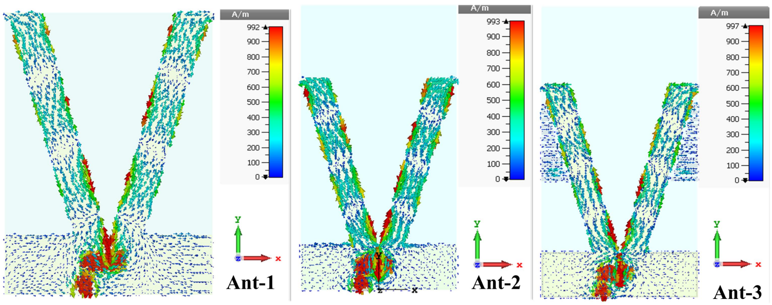

Fig. 9: Surface current distribution of ANT-1 at 0.608-THz (left-most), ANT-2 at 0.71-THz (middle) and ANT-3 at 0.71 (right-most)

In addition to determining the effect of the extension of a dielectric substrate and employing GNR on antenna gain improvement, E-field intensity distribution at different resonance frequencies, i.e., at 0.608 THz, 0.713 THz, and 0.709 THz, as seen in Fig. 10. It can be distinctly exhibited that the main beam of ANT-3 is stronger than ANT-2 due to the employed GNR technique. As a result, it causes relatively higher antenna gain (see Fig. 8). On the other hand, ANT-1 shows smaller strength than ANT-2 and ANT-3, which would cause a smaller gain.

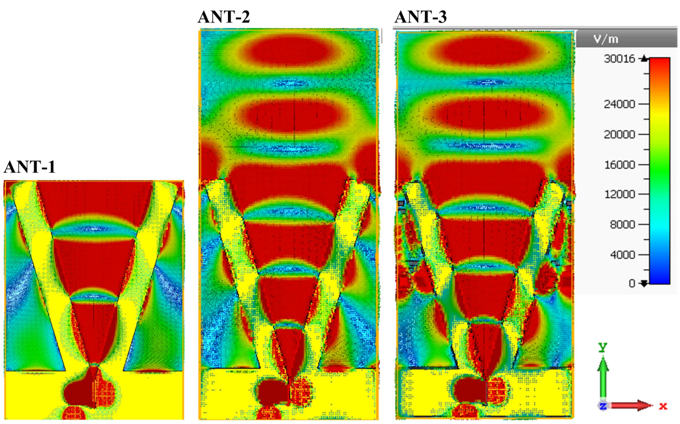

Fig. 10: Electric-field propagation on XY-plane for ANT-1 at 0.61 THz, ANT-2 at 0.71-THz, and ANT-3 at 0.71-THz

Fig.11 reveals the radiation pattern (E-plane) for ANT-3. As displayed in Fig.11(a) the beam width of 61.1^0 and side-lobe level (SLL) of -8.1 dB at 0.55-THz frequency. Also, in Fig. 11 (b) shows the beam width of 59.3^0 and SLL of -7.9 dB at 0.59-THz. Besides, beam width of 46.3^0 and SLL of -11.3 dB at 0.71-THz in Fig. 11 (c). Likewise, Fig. 11 (d) observes beam width of 38.5^0 and SLL of -10.8 dB at 0.85-THz.

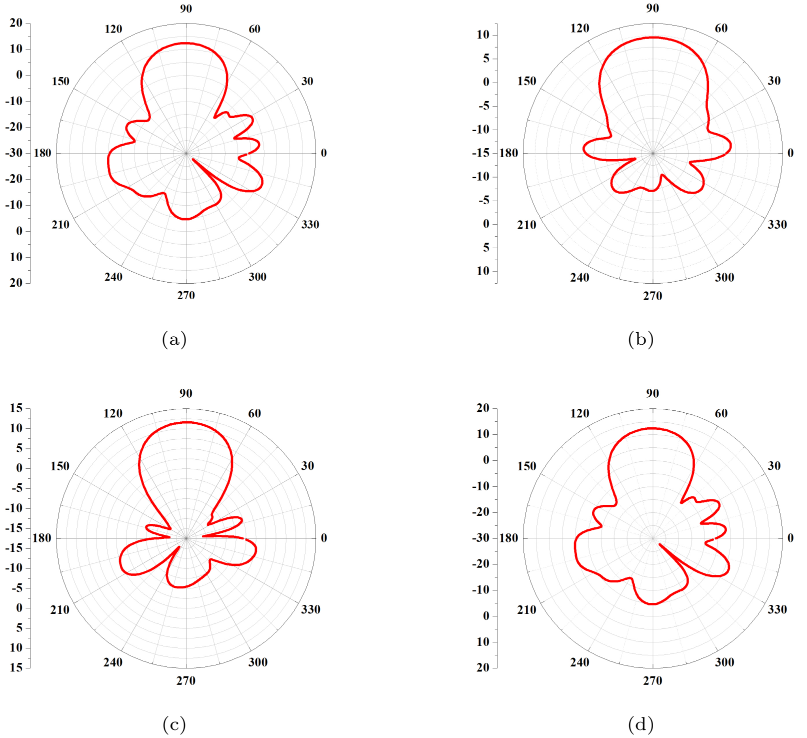

Fig. 11: Radiation pattern of GNR Vivaldi antenna (ANT-3) in E-plane at (a) 0.55 THz (b) 0.59 THz (c) 0.71-THz (d) 0.85 THz

Finally, the proposed antenna is compared with the existing antenna and illustrated in Table 1. The proposed antenna is significantly superior in comparison to gain, directivity, and radiation efficiency.

5 Conclusion

In this study, TSA has been firstly designed and then enhanced the radiation characteristics by substrate extension techniques. Graphene FDTD modeling has been performed to investigate surface current, and E-H filed components. Further, the tunning property has been observed by placing a GNR over the

Table 2: Performance comparison of proposed antenna with existing antenna

Ref.	Operating frequency band (THz)	Impedance Bandwidth (%)	Gain (dBi)	Directivity (dBi)	Radiation efficiency (%)	Recon-figurable
[13]	1-6	~142	-1.6	7.8	16.3	No
[15]	0-0.7	~104	7	–	–	Yes
[16]	0.2-2	~66.7	11.7	–	–	Yes
This work	**0.5-0.9**	**28.49**	**9.59**	**10**	**89.90**	**No**
		14.78	**10.48**	**12.2**	**90.58**	**No**
		41.5	**12.31**	**13.1**	**83.63**	**Yes**

metal structure of Vivaldi and the nearby flared arm structure. It is demonstrated that reflection coefficient, impedance bandwidth, Gain, and radiation efficiency are considerably reconfigurable by varying the chemical potential via field bias. Moreover, this analysis shows that the proposed GNR-based TSA has more impedance bandwidth, Gain, and directivity than conventional TSA in the operating frequency band. The reconfigurable characteristic of the projected method gives more opportunities to study different applications in THz bands, including wireless communication, security, and medical imaging.

Author Declarations

- **Declarations Ethics Approval and Consent to Participate:** Not applicable.
- **Consent to participate:** Not applicable.
- **Consent for Publication:** The manuscript entitled "GNR Based UWB Reconfigurable Tapered Vivaldi Antenna for THz band Applications" has not been published elsewhere. Also, it has not been submitted for publication simultaneously for any other Journals.
- **Availability for data and materials:** Not applicable.
- **Competing Interests:** The author has no related nonfinancial or financial concerns to reveal.
- **Funding:** Not applicable.
- **Authors' Contributions:** Author has studied the design concept, manuscript preparation, proof reading, and all other investigation by his owns.

- **Acknowledgements:** Author would like to acknowledge Chandigarh university Mohali (Punjab) India to provide all the necessary facilities to accomplish this work.

References

[1] T. Wu, T. S. Rappaport, C. M. Collins. Safe for Generations to Come: Considerations of Safety for Millimeter Waves in Wireless Communications[J]. IEEE Microwave Magazine, 2015, 16(2): 65-84

[2] F. Zhu, W. Hong, W. F. Liang, et al. A Low-Power Low-Cost 45-GHz OOK Transceiver System in 90-nm CMOS for Multi-Gb/s Transmission[J]. IEEE Transactions on Microwave Theory and Techniques, 2014, 62(9): 2105-2117.

[3] E. Peytavit, J. F. Lampin, T. Akalin, et al. Integrated terahertz TEM horn antenna [J].Electronics Letters, 2007, 43:73-75.

[4] M. E. Nawawy, A. M. M. A. Allam, M. Ghoneima. Design and fabrication of W-band SIW horn antenna using PCB process[C]. 1st International Conference on Communications, Signal Processing, and their Applications, Sharjah, 2013, 1-3.

[5] T. Tajima, H. J. Song, A. Katsuhiro, et al.300-GHz Step-Profiled Corrugated Horn Antennas Integrated in LTCC[J]. IEEE Transactions on Antennas and Propagation, 2014, 62:5437-5444.

[6] Wu J, Zhao Z, Nie Z, Liu QH. A printed UWB vivaldi antenna using stepped connection structure between slotline and tapered patches. IEEE Antennas Wirel Propag Lett. 2014;13:698-701.

[7] Gibson, P. The Vivaldi Aerial. In Proceedings of the 9th European Microwave Conference, Brighton, UK, 17–20 September 1979; pp. 101–105.

[8] huangshuang Z, Haiwen L, Zhijiao C, Pin W. A compact gain enhanced vivaldi antenna array with suppressed mutual coupling for 5G mmWave application. IEEE Antennas Wirel Propag Lett. 2018;17(5):776-779.

[9] Wang Z, Yin Y, Wu J, Lian R. A miniaturized CPW-fed antipodal Vivaldi antenna with enhanced radiation performance for wide band applications. IEEE Antennas Wirel Propag Lett. 2015;1-1.

[10] Wang YW, Wang GM, Zong BF. Directivity improvement of Vivaldi antenna using double-slot structure. IEEE Antennas Wirel Propag Lett. 2013;12:1380-1383.

[11] De Oliveira AM, Perotoni MB, Kofuji ST, Justo JF. A palm tree antipodal Vivaldi antenna with exponential slot edge for improved radiation pattern. IEEE Antennas Wirel Propag Lett. 2015;14:1334-1337.

[12] Yousaf, Jawad, et al. "Design and analysis of ultra-wideband and high directive THz photoconductive Vivaldi antenna." The Applied Computational Electromagnetics Society Journal (ACES) (2020): 1242-1254.

[13] Dhiflaoui, A., et al. "Design of an ultra-wideband and highly-directive photoconductive THz Vivaldi antenna." 2017 10th Global Symposium on Millimeter-Waves. IEEE, 2017.

[14] Kushwaha, Ritesh Kumar, and P. Karuppanan. "Design and analysis of Vivaldi antenna with enhanced radiation characteristics for mm-wave and THz applications." Optical and Quantum Electronics 51.9 (2019): 1-19.

[15] Jin, Jiangliang, et al. "Reconfigurable terahertz Vivaldi antenna based on a hybrid graphene-metal structure." International Journal of RF and Microwave Computer-Aided Engineering 30.5 (2020): e22175.

[16] Poorgholam-Khanjari, Shima, and Ferdows B. Zarrabi. "Reconfigurable Vivaldi THz antenna based on graphene load as hyperbolic metamaterial for skin cancer spectroscopy." Optics Communications 480 (2021): 126482.

[17] Llatser, Ignacio, et al. "Graphene-based nano-patch antenna for terahertz radiation." Photonics and Nanostructures-Fundamentals and Applications 10.4 (2012): 353-358.

[18] D. L. Sounas and C. Caloz, "Gyrotropy and nonreciprocity of graphene for microwave applications," IEEE Transactions on Microwave Theory and Techniques, vol. 60, no. 4, pp. 901–914, 2012.

[19] C. Sirtori, "Applied physics: Bridge for the terahertz gap," Nature, vol. 417, no. 6885, pp. 132–133, 2002.

[20] W. J. Buchanan, N. K. Gupta and J. M. Arnold, "Simulation of radiation from a microstrip antenna using three-dimensional finite-difference time-domain (FDTD) method", Eighth International Conference on Antennas and Propagation,vol.2, Ed inburgh, UK, 1993, pp. 639-642.

[21] Van Quang, Vu, et al. "Graphene-coated quartz crystal microbalance for detection of volatile organic compounds at room temperature." Thin Solid Films 568 (2014): 6-12

[22] Chen, Xu-Dong, et al. "High-quality and efficient transfer of large-area graphene films onto different substrates." Carbon 56 (2013): 271-278.

[23] K. Yee, "Numerical solution of initial boundary value problems involving maxwells equations in isotropic media", IEEE Transactions on Antennas and Propagation, 14, no. 3 (1966) : 802–807.

[24] S. D. Gedney, "An anisotropic PML absorbing media for the FDTD simulation of fields in lossy and dispersive media", Electromagnetics, 16, no. 4,(1996): 399–415.